analytical chemistry

pubs.acs.org/ac

Article

Ag Nanoparticles with Ultrathin Au Shell-Based Lateral Flow Immunoassay for Colorimetric and SERS Dual-Mode Detection of SARS-CoV-2 IgG

Penghui Liang, Qi Guo, Tianyu Zhao, Cong-Ying Wen,* Zhangyu Tian, Yanxue Shang, Jinyan Xing, Yongzhong Jiang, and Jingbin Zeng*

Cite This: *Anal. Chem.* 2022, 94, 8466−8473

Read Online

ACCESS | Metrics & More | Article Recommendations | Supporting Information

ABSTRACT: Immunoglobulin detection is essential for diagnosing progression of SARS-CoV-2 infection, for which SARS-CoV-2 IgG is one of the most important indexes. In this paper, Ag nanoparticles with ultrathin Au shells (~2 nm) embedded with 4-mercaptobenzoic acid (MBA) (Ag^{MBA}@Au) were manufactured via a ligand-assisted epitaxial growth method and integrated into lateral flow immunoassay (LFIA) for colorimetric and SERS dual-mode detection of SARS-CoV-2 IgG. Ag^{MBA}@Au possessed not only the surface chemistry advantages of Au but also the superior optical characteristics of Ag. Moreover, the nanogap between the Ag core and the Au shell also greatly enhanced the Raman signal. After being modified with anti-human antibodies, Ag^{MBA}@Au recognized and combined with SARS-CoV-2 IgG, which was captured by the SARS-CoV-2 spike protein on the T line. Qualitative analysis was achieved by visually observing the color of the T line, and quantitative analysis was conducted by measuring the SERS signal with a sensitivity four orders of magnitude higher (detection limit: 0.22 pg/mL). The intra-assay and inter-assay variation coefficients were 7.7 and 10.3%, respectively, and other proteins at concentrations of 10 to 20 times higher than those of SARS-CoV-2 IgG could hardly produce distinguishable signals, confirming good reproducibility and specificity. Finally, this method was used to detect 107 clinical serum samples. The results agreed well with those obtained from enzyme-linked immunosorbent assay kits and were significantly better than those of the colloidal gold test strips. Therefore, this dual-mode LFIA has great potential in clinical practical applications and can be used to screen and trace the early immune response of SARS-CoV-2.

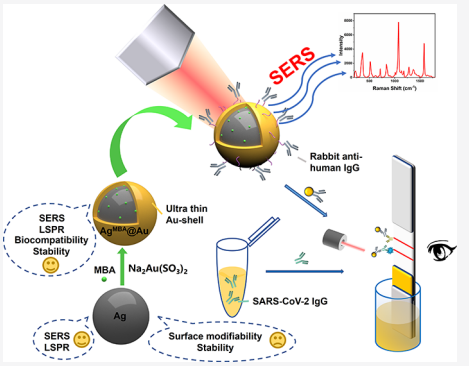

INTRODUCTION

The 2019 novel coronavirus disease (COVID-19) is caused by severe acute respiratory syndrome coronavirus 2 (SARS-CoV-2) and has now spread globally.[1] By the end of November 2021, hundreds of millions of people had been infected and millions had died. SARS-CoV-2 is highly contagious and spreads mainly through droplets in the air medium.[2−4] Currently, the real-time reverse transcription polymerase chain reaction (RT-PCR) is the standard test for SARS-CoV-2 diagnosis.[5,6] The method has the advantages of high sensitivity and accuracy but requires complex procedures and expensive equipment, which makes it difficult to implement in countries or regions with limited resources.

Serological tests mainly for IgG and IgM antibodies are good complements of RT-PCR for SARS-CoV-2 diagnosis. Studies have revealed that supplemental antibody testing can effectively improve the accuracy of diagnosis.[7,8] Compared with nucleic acid detection, antibody detection has shorter turnaround time, lower cost and technical requirements, and lower risk of infection.[9] Moreover, serological test is the essential link to accurately diagnose the disease progression of SARS-CoV-2 infection, which helps to provide guidance for choosing suitable treatment and evaluate the treatment effect.[10,11] Besides, IgG detection helps to study the mechanism of infection.[12] At present, enzyme-linked immunosorbent assay (ELISA)[13] and chemiluminescence immunoassay (CI)[14] are the main clinical methods for detection of antibodies. These methods have acceptable sensitivity and quantification advantages. However, they are not suitable for on-site and in-time testing or screening due to the fact that they rely on centralized laboratory infrastructure with troublesome sample transportation logistics and operational procedures.

Lateral flow immunoassay (LFIA) has gained widespread attention since its emergence. It has the advantages of speed, portability, cost-effectiveness, convenience, and moreover, the

Received: March 23, 2022
Accepted: May 19, 2022
Published: June 3, 2022

results can be read directly with naked eyes. Therefore, LFIA is currently the most promising format for on-site instant diagnosis. LFIA has been used in the detection of metal ions, small molecules, nucleic acids, and proteins.[15] However, this method suffers from two main drawbacks of low sensitivity and difficulty in accurate quantification. This is mainly attributed to the application of colloidal gold as a reporter. In recent years, researchers have tried to develop various nanobeacon materials to replace colloidal gold, including fluorescent microspheres,[16] up-conversion luminescence materials,[17,18] quantum dots,[19,20] and magnetic particles,[21,22] and so on. Among them, surface-enhanced Raman scattering (SERS) nanotags can provide strong fingerprint signals and have been combined with the LFIA platform to develop ultrasensitive indicators for trace biological substances.[23−25]

SERS nanotags are usually composed of noble metal nanoparticles (NPs). When Raman-active molecules are adsorbed on or near the surface of SERS nanotags, their Raman signals can be significantly enhanced. As a typical SERS substance in biological analysis, Au NPs possess the advantages of excellent stability and biocompatibility, but their SERS activity is typically orders of magnitude lower than that of Ag NPs.[26,27] In contrast, Ag NPs possess superior SERS activity and high molar absorption coefficients but suffer from low stability and poor surface functionalization. An alternative to address this issue is to uniformly coat an ultrathin layer of Au on the Ag cores, endowing the particles with gold's surface chemistry and silver's optical characteristics. A main challenge to this strategy is that the addition of tetrachloroaurate ($AuCl_4^-$) inevitably results in the etching of Ag cores during the coating process because the electric potential of $AuCl_4^-$/Au (1.002 V vs standard hydrogen electrode, SHE) is higher than that of Ag^+/Ag (0.7996 V vs SHE). Thus, the hollowing of Ag cores and the alloying of Au shells occur simultaneously,[28,29] which greatly reduces their SERS performance.

Inspired by pioneer research and our previous work,[30−32] we propose a ligand-assisted epaxial growth method to deposit an ultrathin layer of Au on Ag cores without etching them. By complexing tetrachloroaurate with sulfite, its oxidative potential is significantly lowered to 0.111 V versus SHE, preventing its oxidative etching towards Ag cores. By this approach, an efficient SERS probe structure with Ag NPs as cores, ultrathin Au as shells (~2 nm), and 4-mercaptobenzoic acid (MBA) embedded in the gap as the Raman reporter (Ag^{MBA}@Au) was constructed. This particle can actually be considered as a "quasi-silver" material with gold-like surface chemistry. The ultrathin Au shell is conducive to the combination with biomolecules, protects the internal silver core, and prevents Raman reporter molecules from external influence, so as to improve the biocompatibility, chemical, and signal stability of particles. In addition, the enhanced plasma formed by the gap between the Au shell and the Ag core can produce a strong electromagnetic field, which has a stronger enhancement effect than the traditional nanolabel.[33] We integrated this SERS reporters into LFIA and achieved colorimetric and SERS dual-mode detection of SARS-CoV-2 IgG. Due to the strong SERS signal and high stability of this probe, the SERS-based LFIA achieved a sensitivity four orders of magnitude higher than that of the visual method and showed good specificity, reproducibility, and anti-interference ability. Finally, this method was successfully applied to the actual serum samples, and the results matched well with those of commercially available ELISA kits and were significantly better than those of the commercially available colloidal gold test strips.

EXPERIMENT SECTION

Synthesis of Ag^{MBA}@Au NPs. Ag seeds and Ag NPs were first synthetized based on the citrate reduction method.[34] The detailed procedure is given in the Supporting Information. The procedure for coating of Au shells is described below.[30] 50 μL of 0.029 M $HAuCl_4$, 0.24 mL of 0.20 M NaOH, and 3.0 mL of 0.010 M Na_2SO_3 were added to 4.7 mL of ultrapure water and left standing in the dark for 12 h to obtain a colorless and transparent growth solution. Subsequently, 5.0 mL of 5.0% PVP solution, 50 μL of 0.50 M L-ascorbic acid (L-AA) solution, 0.20 mL of 0.50 M NaOH, and 0.20 mL of 0.10 M Na_2SO_3 were sequentially added to 4 mL of the above Ag NP sol. After sonication for 10 min, 1.0 mL of growth solution was added to the solution, which was allowed to stand at 65 °C for 1 h. The obtained NPs were washed by centrifugation with ultrapure water and dispersed in 10 mL of water. The complete synthesis and functionalization process are shown in Figure 1a.

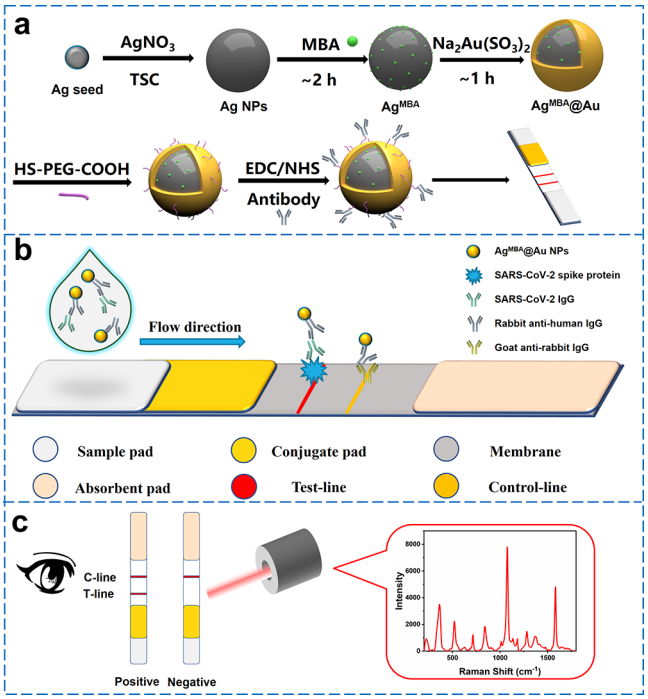

Figure 1. (a) Flow chart of synthesis and functionalization of Ag^{MBA}@Au NPs. (b) Schematic diagram of the test strip structure and detection principle. (c) Interpretation of the detection results.

Functionalization of Ag^{MBA}@Au with Anti-Human Antibodies. 10 mL of Ag^{MBA}@Au NPs was added to 5.0 mL of 3.0 mg/mL HS-(PEG)*n*-COOH solution and reacted under vigorous stirring at room temperature for 2 h. Then, Ag^{MBA}@Au NPs were washed three times by centrifugation and dispersed in 1.0 mL of PBS (10 mM pH = 6.8). 50 μL of 20 mg/mL 1-(3-dimethylaminopropyl)-3-ethylcarbodiimide hydrochloride and 50 μL of 10 mg/mL *N*-hydroxysuccinimide were sequentially added to the above solution, followed by gentle shaking at room temperature for 30 min. Then, the Ag^{MBA}@Au NPs were washed twice and dispersed in 1 mL of PBS (10 mM pH = 7.4) with the addition of 10 μg of rabbit anti-human antibodies. The reaction lasted for 2 h. Finally, the

https://doi.org/10.1021/acs.analchem.2c01286
Anal. Chem. 2022, 94, 8466−8473

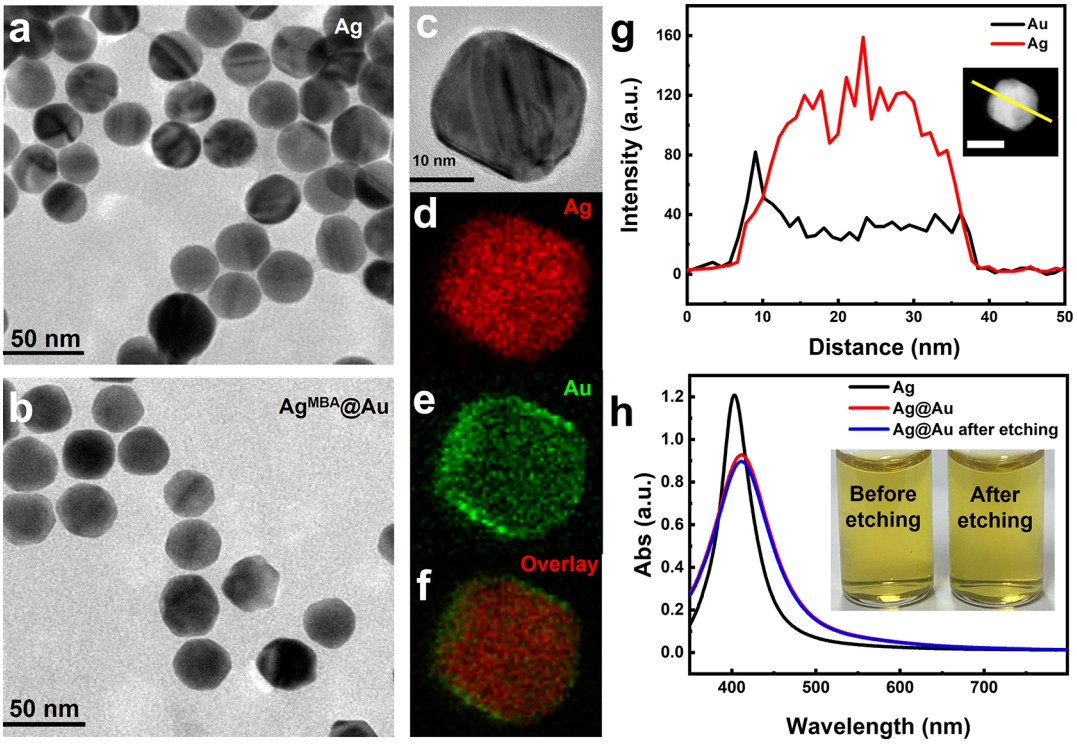

Figure 2. Characterization of Ag^{MBA}@Au NPs. (a,b) TEM images of Ag and Ag^{MBA}@Au NPs. (c) HR-TEM images of a single Ag^{MBA}@Au NP. (d–f) EDX element mappings of Ag, Au, and their overlay. (g) EDX line scan image of Ag^{MBA}@Au NPs, and the inset shows the line scan area image. (h) UV–vis spectra of Ag and Ag^{MBA}@Au before and after etching, and the inset shows the photographs of Ag^{MBA}@Au NPs before and after etching.

obtained immunonanoparticles (INPs) were washed with PBS, blocked by BSA, dispersed in 1.0 mL of 10 mM pH = 7.4 PBS containing 0.5% Tween-20, 1.0% BSA, and 1.0% sucrose, and stored at 4 °C.

Fabrication of LFIA Strips. As shown in Figure 1b, NC membranes, sample pads, conjugate pads, and absorbent pads were pasted on the PVC substrate to constitute the test strip. The T line was sprayed with 1.0 mg/mL spike protein at a spray rate of 1.0 μL/cm, and the control line (C line) was sprayed with 1.0 mg/mL goat anti-rabbit antibodies at a spray rate of 1.0 μL/cm.[35−38] The LFIA test strips were dried at 37 °C for 24 h and cut into 3 mm width, which were stored at 25 °C. Before use, 50 μL of blocking solution (1.0% Tween-20 and 0.5% BSA in pH = 7.4 PBS) was added to the sample pad to block the test strip and dried for several hours at room temperature to dryness.

Detection of SARS-CoV-2 IgG. The analysis of SARS-CoV-2 IgG by the dual-mode LFIA was performed as follows. In a microtiter plate, 40 μL of SARS-CoV-2 IgG sample and a certain amount of INPs were mixed and sequentially added with the running solution (1.0% Tween-20 and 1.0% BSA in pH = 7.4 PBS) to make the final total volume reach 100 μL. After a period of time, the sample pad of the LFIA test strip was immersed in the mixed solution. After 15 min, by visually observing the color of the T line, qualitative detection was achieved. Meanwhile, a portable Raman spectrometer with a 785 nm laser was used to measure the Raman peak intensity, and the intensity of the peak at 1075 cm^{-1} was acquired for quantitative detection.

Application to Simulated Serum Samples and Clinical Samples. Simulated serum samples were prepared by spiking different concentrations of SARS-CoV-2 IgG in serum of healthy volunteers. The samples were diluted 10 times with PBS and then tested with dual-mode LFIA following the procedure described. For clinical samples, blood taken from 98 vaccinated and 9 unvaccinated volunteers was kept overnight at 2–8 °C and then centrifuged at 1000*g* for 20 min at 2–8 °C before detection. In addition, each clinical sample was also tested using commercially available ELISA kits and colloidal gold test strips according to the instructions.

RESULTS AND DISCUSSION

Principle of Dual-Mode Strips-Based Detection of SARS-CoV-2 IgG. Figure 1b illustrates the basic structure and working principle of the dual-mode strips. The assay was based on antigen–antibody reaction. INPs recognized and bound with SARS-CoV-2 IgG, which was captured by the SARS-CoV-2 spike protein on the T line to form a sandwich structure. As a result, INPs assembled on the T line, producing a colored band, while free INPs moved further and were trapped by the goat anti-rabbit antibodies on the C line for quality control. The determination of the results is illustrated in Figure 1c. The sample was considered positive when two colored bands appeared on the T line and the C line and negative when only the C line was seen, and the other results were invalid. For qualitative detection, naked eyes were used to observe the color bands due to the localized surface plasmon resonance effect of the INPs. For quantitative detection, the SERS signal could be measured using a portable Raman spectrometer. The dual-signal readout of INPs enabled visual-qualitative and instrument-quantitative analyses.

Characterization of Ag^{MBA}@Au NPs. To avoid the etching of Ag cores during Au coating, a ligand-assisted

https://doi.org/10.1021/acs.analchem.2c01286
Anal. Chem. 2022, 94, 8466−8473

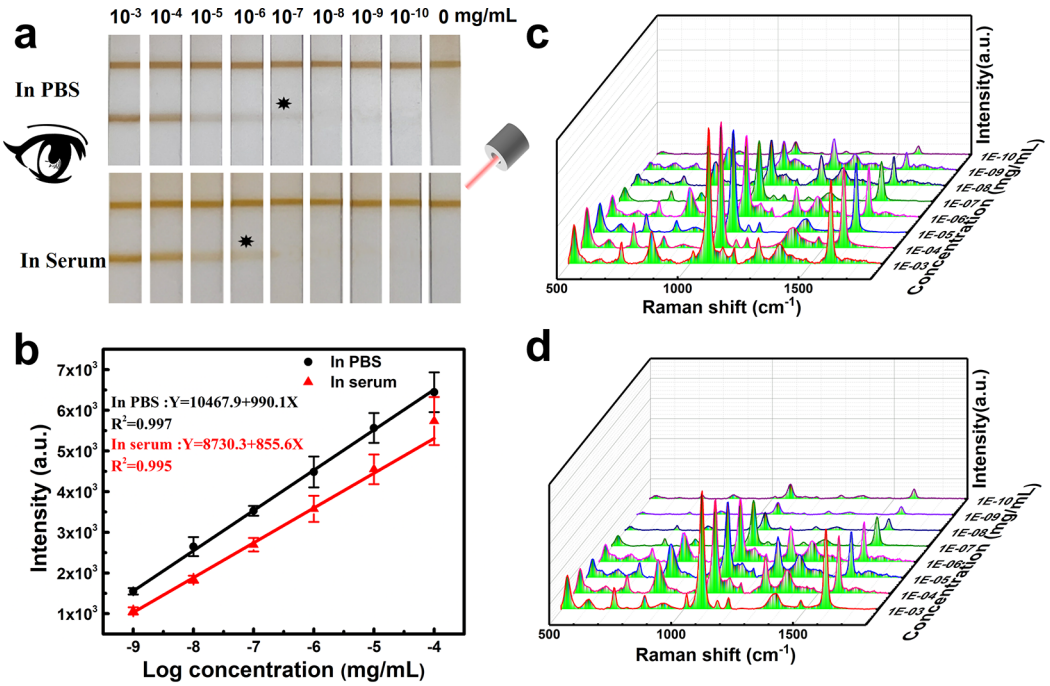

Figure 3. (a) Photographs of test strips obtained from PBS and serum samples with different concentrations of SARS-CoV-2 IgG (the asterisk represents the detection limit with naked eyes). (b) Linear response for SARS-CoV-2 IgG detection at the concentration from 10^{-9} to 10^{-4} mg/mL in PBS and serum. Error bars were calculated from three experiments. (c,d) Raman spectra obtained from (c) PBS and (d) serum samples with different concentrations of SARS-CoV-2 IgG.

complexing approach was employed by using sodium sulfite as the complexing and reducing agent, which could lower the oxidative potential of $HAuCl_4$ by forming a highly stable complex of gold (I) sulfite, $Na_2Au(SO_3)_2$ (pK_{sp} = −26.8). As shown in Figures 2a,b and S1, the diameter of Ag NPs was about 30 nm, and after being coated with Au shells, their sizes increased to 32 nm. HR-TEM and EDX characterizations of a single Ag^{MBA}@Au are shown in Figure 2c−f. It could be seen that the Ag element was mainly distributed inside the particles and Au was mainly distributed on the outer periphery. The EDX line scan of Ag^{MBA}@Au (Figure 2g) showed that along the trajectory of the yellow line, the Ag element appeared in the middle part with a higher intensity. The Au element appeared at the beginning and the end part with weak intensity, and the distribution range was slightly beyond the Ag element. The above results demonstrated that Ag^{MBA}@Au NPs had a Ag core and an ultrathin Au shell. Compared with Ag NPs, the characteristic absorption of Ag^{MBA}@Au NPs redshifted from 402 to 408 nm (Figure 2h), which was attributed to an increase in the local dielectric constant caused by Au coating.[30] This also confirmed that Au was coated on Ag with ultrathin thickness, which hardly influenced the optical characteristics of Ag. Furthermore, we investigated the stability of Ag^{MBA}@Au by H_2O_2 etching. In the etching experiments, we used H_2O_2 with a final concentration of 1.0% to incubate Ag and Ag^{MBA}@Au with the same colloidal concentration for 24 h. As shown in Figure 2h, the UV−vis spectrum of Ag^{MBA}@Au NPs hardly changed after etching and the color of Ag^{MBA}@Au NP solution also remained the same. At this concentration of H_2O_2, Ag NPs were completely etched, their absorption peak disappeared, and their solution turned to colorless (Figure S2a). This demonstrated that such an ultrathin Au shell produced a distinct protective effect on Ag NPs, which was beneficial for their further biological application. We also tried Ag^{MBA}@Au NPs with different shell thicknesses. The TEM image, particle size distribution map, and etching experiment are shown in Figures S2b,c and S3. It could be seen that the 2 nm Au shell is the lowest thickness that could maintain stability. Finally, we compared the SERS performance of Ag^{MBA} and Ag^{MBA}@Au. As shown in Figure S4, the signal generated by Ag^{MBA}@Au was significantly stronger than that generated by Ag^{MBA}. This indicated that the thin Au shell not only protected the Ag core but also significantly enhanced the SERS performance of Ag. This might be because the gap between Ag and Au generated a significantly higher electromagnetic field than that of the surface of Ag, which greatly increased the SERS performance of Ag^{MBA}@Au.[39] In the SERS spectra, the strong bands at 713, 846, 1360, 1584, and 1075 cm^{-1} were assigned to ν(OCO) vibration, δ(OCO) vibration, $\nu(COO^-)$ vibration, ν(CC) vibration, and ν(CS) aromatic ring characteristic vibrations. Among them, the ν(CS) band had good concentration dependence.[40,41] Therefore, we chose the 1075 cm^{-1} Raman peak for quantitative analysis.

Biomodification of Ag^{MBA}@Au NPs. Biomodification of Ag^{MBA}@Au NPs was performed with carbodiimide chemistry. To confirm the conjugation, the obtained INPs were reacted with Alexa Fluor 647-labeled goat anti-rabbit antibodies. As shown in Figure S5a, the largest fluorescence peak (667 nm) of Alexa Fluor 647 was observed with INPs. Although the Ag^{MBA}@Au NPs were treated with goat anti-rabbit antibodies labeled with Alexa Fluor 647, no Alexa Fluor 647 fluorescence appeared. This indicated that the rabbit anti-human antibodies were successfully coupled with Ag^{MBA}@Au NPs. In addition, the modification had a little effect on the optical and morphology properties of the nanoparticles. Their absorption spectra and TEM images (Figure S5b−d) showed that the absorption peak of INPs redshifted slightly, the solution color remained the same, and the particle size changed little.

https://doi.org/10.1021/acs.analchem.2c01286
Anal. Chem. 2022, 94, 8466−8473

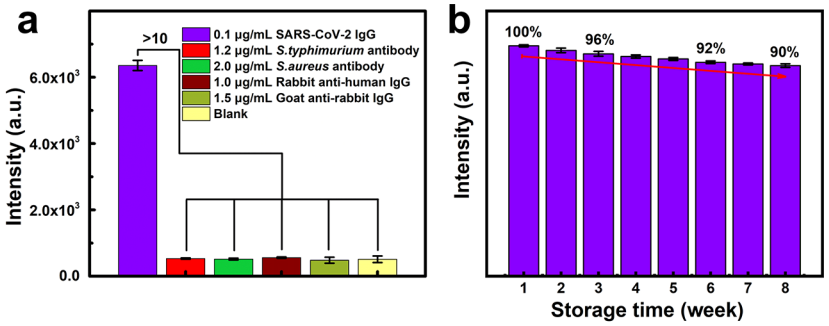

Figure 4. (a) Histogram of Raman signal intensities obtained from serum samples spiked with different proteins and the blank samples with the dual-mode LFIA method. (b) Histogram of Raman signal intensities obtained from SARS-CoV-2 IgG samples with the dual-mode LFIA method using Ag^{MBA}@Au stored at different times. Error bars were calculated from three experiments.

Analytical Performance of the Dual-Mode Strips for SARS-CoV-2 IgG Detection. We first optimized the detection conditions such as the BSA concentration in the blocking solution, the reaction time, the amount of the INPs, and the amount of conjugated antibodies (Figure S6a−e). Finally, 10% BSA, 5 min reaction, 20 μL of probe solution, 10 μg of antibody, and 1 μg/cm were selected. Under optimal conditions, we investigated the sensitivity and dynamic range of this method. As shown in Figure 3a, when there was no SARS-CoV-2 IgG in PBS samples, only the C line could be observed under natural light. As the concentration of SARS-CoV-2 IgG increased to 10^{-7} mg/mL, the T line began to generate color, and with the increase in the SARS-CoV-2 IgG concentration, the number of INPs bound with SARS-CoV-2 IgG increased. Finally, the T line captured more INPs and exhibited darker colors. By observing the color change of the T line, the sample could be qualitatively and semi-quantitatively detected. In serum samples, until the SARS-CoV-2 IgG concentration reached 10^{-6} mg/mL, the color band could be obviously identified, which might be due to the complex matrix of the serum. For accurate quantification, the SERS spectra of the T line were collected. As shown in Figure 3c,d, the Raman scattering peak gradually increased with the increasing concentration. The intensity of the maximum scattering peak at 1075 cm^{-1} was measured for quantitative analysis. It was worth noting that an irregular scattering peak appeared at 1282 cm^{-1} in the SERS spectra. To investigate this phenomenon, we measured the Raman spectra of 14 nitrocellulose membranes individually. Figure S7a shows that the peaks at 1282 and 840 cm^{-1} were the background signals of the nitrocellulose membranes, but they appeared in some cases and disappeared in other cases. This might be attributed to the quality differences among different batches of NC membranes. However, these background signals hardly influenced the detection accuracy. Figure S7b,c,d shows the data of intra-assay in the reproducibility experiment. It could be seen that no matter whether the 1282 cm^{-1} peak appeared or not, the intensities of 1075 cm^{-1} peaks were nearly the same. The coefficients of variation (CVs) for PBS samples with 10^{-4}, 10^{-5}, and 10^{-6} mg/mL SARS-CoV-2 IgG were 7.3, 7.4, and 8.4%, respectively, indicating that this method had good reproducibility, which further proved that the 1282 cm^{-1} background signals hardly influenced the detection accuracy. As shown in Figure 3b, the assay exhibited a good and wide linear range at the concentration from 10^{-9} to 10^{-4} mg/mL both in PBS and serum. The detection limits were respectively calculated to be 0.22 and 0.52 pg/mL based on the lowest distinguishable signal (the average signal of blank samples added with their three times standard deviation, n = 12). It could be seen that the SERS-based test in PBS and serum had nearly the same dynamic range and sensitivity, indicating that the use of Raman spectroscopy for detection had good anti-interference ability.

A comparison of different biosensors used to detect SARS-CoV-2 IgG[25,35,42−52] is listed in Table S1. Compared with the current clinical methods including ELISA and CI, LFIA took much less time. Moreover, LFIA could be accomplished conveniently, and the results could be read with naked eyes or a portable instrument. These advantages made LFIA have a great application value in areas with poor medical conditions. Among them, SERS-based LFIA showed a much lower detection limit compared with those using other labels. In particular, the detection limit of our assay reached 0.52 pg/mL, which could be compared with the LFIA using Au nanostars (the lowest detection limit reported up to now).[52] However, using Au nanostars could not generate good quantification signals, while our method showed the widest linear range. The good analytical performance of our method was mainly due to the excellent SERS performance and stability of Ag^{MBA}@Au NPs. These results indicated that Ag^{MBA}@Au NPs were a good marker and had great potential in sensitive and quantification detection.

Specificity, Stability, and Reproducibility. We further investigated the specificity and reproducibility of this method. We used several common antibodies to study the specificity of this method (Figure 4a). It could be seen that 0.1 μg/mL SARS-CoV-2 IgG could produce a strong signal, while other proteins (*Salmonella typhimurium* antibodies, *Staphylococcus aureus* antibodies, rabbit anti-human IgG, and goat anti-rabbit antibodies) did not produce obvious signals with concentrations even 10−20 times higher, which were not much different from those of the blank samples. This suggested that the method had good specificity. On the other hand, the temperature effects on the detection and storage of the test strips were investigated. As shown in Figure S8, there was no significant difference in the signals detected with the freshly prepared strips at different operation temperatures from 4 to 40 °C. After 1 week of storage at 4, 25, 37, and 40 °C, the detection efficiency remained 98, 97, 98, and 75% of the original value with the CV of 3.6, 4.3, 6.7, and 9.8%, respectively. We further performed long-term stability tests at 25 °C. Figure 4b shows the detection signals from the same samples detected with INPs and strips stored for different times. It could be seen that with the extension of the storage

https://doi.org/10.1021/acs.analchem.2c01286
Anal. Chem. 2022, 94, 8466−8473

time, the detection signal decreased slightly, and the signal intensity could still be maintained nearly 90% after 8 weeks. This proved that the INPs had good stability. Furthermore, we studied the intra-assay and inter-assay CV of this method in PBS and serum (Tables 1 & 2). The intra-assay CV was calculated by using the same batch of INPs, and inter-assay CV was calculated by using the different batches of INPs. The intra-assay CV in PBS and serum was 7.7 and 9.1%, respectively, and the inter-assay CV in PBS and serum was 10.6 and 13.2%, respectively, indicating that this method had good reproducibility. Overall, the above results proved that our method had good specificity, reproducibility, and stability, which was mainly due to the protective effect of the Au shell on the Ag core and the Raman reporter.

Table 1. Reproducibility Test of the Dual-Mode Test Strips in PBS Solution

IgG concentration (mg/mL)	intra-assay			inter-assay		
	mean	SD	CV (%)	mean	SD	CV (%)
10^{-4}	6484	471	7.3	6493	759	11.6
10^{-5}	5261	389	7.4	5487	570	10.4
10^{-6}	4294	361	8.4	4151	407	9.8
intra-assay variability 7.7%				inter-assay variability 10.6%		

Table 2. Reproducibility Test of the Dual-Mode Test Strips in Serum

IgG concentration (mg/mL)	intra-assay			inter-assay		
	mean	SD	CV (%)	mean	SD	CV (%)
10^{-4}	5734	590	10.3	5433	723	13.3
10^{-5}	4549	365	8.0	4378	601	13.9
10^{-6}	3576	321	9.0	3789	472	12.5
intra-assay variability 9.1%				inter-assay variability 13.2%		

Clinical Sample Tests. This method was applied to the detection of SARS-CoV-2 IgG in the serum of 98 vaccinated and 9 unvaccinated volunteers. The results are shown in Figures 5a, S9−S18, and Tables S2−S3. The case where the T line color could be seen clearly was "strong positive". "Weak positive" referred to the cases where the T line could hardly be observed with the naked eye but could be read out with a portable Raman spectrometer. "Negative" meant below the detection limit. In the samples from the vaccinated volunteers, we found 26 cases of strong positive, 6 cases of weak positive, and 66 cases of negative. The samples of unvaccinated volunteers were all negative. In order to verify the accuracy of our method, we simultaneously tested the above clinical samples with the commercially available ELISA kit and colloidal gold test strips (Figure 5b, Tables S2&S3). For vaccinated samples, 34 cases were tested positive with ELISA kits and 11 cases were tested positive with colloidal gold test strips. For samples not being vaccinated, all cases were tested negative. Through comparison, it was found that the detection results of our method were similar to those of the commercial ELISA kits and significantly better than those of the colloidal gold test strips.

CONCLUSIONS

In the current study, we developed a Ag^{MBA}@Au NP-based dual-mode LFIA method for qualitative analysis of SARS-CoV-2 IgG with naked eyes and quantitative detection by Raman spectroscopy. Ag^{MBA}@Au NPs had Ag cores with ultrathin Au shells, which exhibited an excellent SERS effect and good stability and biocompatibility. The SERS-based LFIA had strong anti-interference ability and could achieve ultra-sensitive detection with an LOD of 0.52 pg/mL in serum samples, which was four orders of magnitude lower than that of the visual observation. Besides, the method has the advantages of simple operation, time efficiency, and excellent stability, specificity, and reproducibility. Finally, this method was successfully applied to the actual serum samples. The detection results matched well with those of commercially available ELISA kits, which were significantly better than those of the colloidal gold test strips. Therefore, this dual-mode LFIA sensor showed great potential in on-site and in-time detection, which is of great significance to countries or regions with limited resources. In our future work, we will gradually optimize detection conditions and preferred antibodies to facilitate the development of dry LFIA. Furthermore, we will try to directly detect whole blood samples instead of serum samples, which will reduce the time for the entire testing process. These improvements will make the operation more convenient and user-friendly.

ASSOCIATED CONTENT

Supporting Information

The Supporting Information is available free of charge at https://pubs.acs.org/doi/10.1021/acs.analchem.2c01286.

Fabrication and characterization of Ag nanoparticles, validation of INPs, optimization of detection conditions,

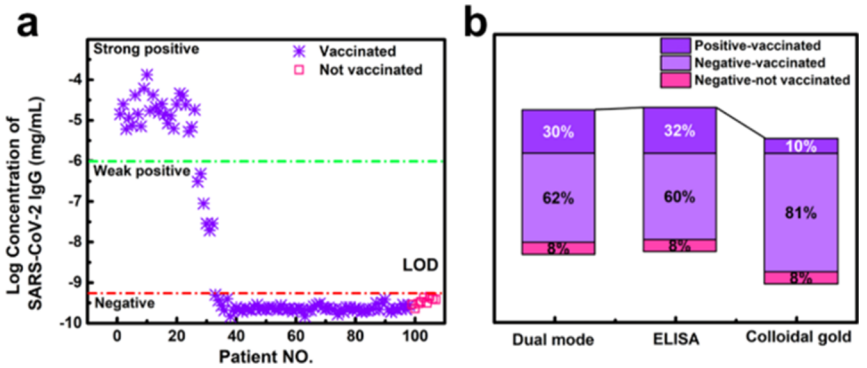

Figure 5. (a) Results of the dual-mode test strips used in actual sample testing. (b) Comparison of the dual-mode test strips with commercially available ELISA kits and colloidal gold test strips.

https://doi.org/10.1021/acs.analchem.2c01286
Anal. Chem. 2022, 94, 8466−8473

and detection results of CFMN-based LFIA for real samples (PDF)

AUTHOR INFORMATION

Corresponding Authors

Cong-Ying Wen − *College of Chemistry and Chemical Engineering, China University of Petroleum (East China), Qingdao 266580, P. R. China;* orcid.org/0000-0002-5471-7694; Email: flcyxt@163.com

Jingbin Zeng − *College of Chemistry and Chemical Engineering, China University of Petroleum (East China), Qingdao 266580, P. R. China;* orcid.org/0000-0002-6179-8867; Email: zengjb@upc.edu.cn

Authors

Penghui Liang − *College of Chemistry and Chemical Engineering, China University of Petroleum (East China), Qingdao 266580, P. R. China*

Qi Guo − *The Affiliated Hospital of Qingdao University, Qingdao University, Qingdao 266003, China*

Tianyu Zhao − *College of Chemistry and Chemical Engineering, China University of Petroleum (East China), Qingdao 266580, P. R. China*

Zhangyu Tian − *College of Chemistry and Chemical Engineering, China University of Petroleum (East China), Qingdao 266580, P. R. China*

Yanxue Shang − *College of Chemistry and Chemical Engineering, China University of Petroleum (East China), Qingdao 266580, P. R. China*

Jinyan Xing − *The Affiliated Hospital of Qingdao University, Qingdao University, Qingdao 266003, China*

Yongzhong Jiang − *Hubei Provincial Center for Disease Control and Prevention, Wuhan 430065, China*

Complete contact information is available at: https://pubs.acs.org/10.1021/acs.analchem.2c01286

Author Contributions

P.L., Q.G., T.Z., and Y.S. designed and performed the experiments. P.L., J.Z., and Congying Wen analyzed the data and wrote the article. J.Z. and Congying Wen conceived the project and supervised the research. J.X., Z.T. and Y.J. analyzed and discussed the data. All authors discussed the results and contributed to the paper.

Notes

The authors declare no competing financial interest.

ACKNOWLEDGMENTS

This work was supported by the Key Fundamental Project of Shandong Natural Science Foundation (Z.J., ZR2020ZD13), the Natural Scientific Foundation of Shandong (W.C., ZR2020MB064), the Science and Technology Projects of Qingdao (Z.J., 21-1-4-sf-7-nsh), the National Natural Science Foundation of China (Z.J., no. 21876206), the Key Research and Development Program of Hubei Province (J.Y., 2020BCA090), and the National Key Research and Development Program of China (J.Y., 2020YFC0840800).

REFERENCES

(1) Zhou, P.; Yang, X.-L.; Wang, X.-G.; Hu, B.; Zhang, L.; Zhang, W.; Si, H.-R.; Zhu, Y.; Li, B.; Huang, C.-L.; Chen, H.-D.; Chen, J.; Luo, Y.; Guo, H.; Jiang, R.-D.; Liu, M.-Q.; Chen, Y.; Shen, X.-R.; Wang, X.; Zheng, X.-S.; Zhao, K.; Chen, Q.-J.; Deng, F.; Liu, L.-L.; Yan, B.; Zhan, F.-X.; Wang, Y.-Y.; Xiao, G.-F.; Shi, Z.-L. *Nature* **2020**, *588*, No. E6.

(2) Wu, Z.; McGoogan, J. M. *JAMA, J. Am. Med. Assoc.* **2020**, *323*, 1239−1242.

(3) Wiersinga, W. J.; Rhodes, A.; Cheng, A. C.; Peacock, S. J.; Prescott, H. C. *JAMA, J. Am. Med. Assoc.* **2020**, *324*, 782−793.

(4) Guan, W.-j.; Ni, Z.-y.; Hu, Y.; Liang, W.-h.; Ou, C.-q.; He, J.-x.; Liu, L.; Shan, H.; Lei, C.-l.; Hui, D. S. C.; Du, B.; Li, L.-j.; Zeng, G.; Yuen, K.-Y.; Chen, R.-c.; Tang, C.-l.; Wang, T.; Chen, P.-y.; Xiang, J.; Li, S.-y.; Wang, J.-l.; Liang, Z.-j.; Peng, Y.-x.; Wei, L.; Liu, Y.; Hu, Y.-h.; Peng, P.; Wang, J.-m.; Liu, J.-y.; Chen, Z.; Li, G.; Zheng, Z.-j.; Qiu, S.-q.; Luo, J.; Ye, C.-j.; Zhu, S.-y.; Zhong, N.-s. *N. Engl. J. Med.* **2020**, *382*, 1708−1720.

(5) Li, Z.; Yi, Y.; Luo, X.; Xiong, N.; Liu, Y.; Li, S.; Sun, R.; Wang, Y.; Hu, B.; Chen, W.; Zhang, Y.; Wang, J.; Huang, B.; Lin, Y.; Yang, J.; Cai, W.; Wang, X.; Cheng, J.; Chen, Z.; Sun, K.; Pan, W.; Zhan, Z.; Chen, L.; Ye, F. *J. Med. Virol.* **2020**, *92*, 1518−1524.

(6) Zhu, X.; Wang, X.; Han, L.; Chen, T.; Wang, L.; Li, H.; Li, S.; He, L.; Fu, X.; Chen, S.; Xing, M.; Chen, H.; Wang, Y. *Biosens. Bioelectron.* **2020**, *166*, 112437.

(7) Carter, L. J.; Garner, L. V.; Smoot, J. W.; Li, Y.; Zhou, Q.; Saveson, C. J.; Sasso, J. M.; Gregg, A. C.; Soares, D. J.; Beskid, T. R.; Jervey, S. R.; Liu, C. *ACS Cent. Sci.* **2020**, *6*, 591−605.

(8) Zalzala, H. H. *New Microbes New Infect.* **2020**, *38*, 100761.

(9) Martín, J.; Tena, N.; Asuero, A. G. *Microchem. J.* **2021**, *167*, 106305.

(10) Maple, P. A. C.; Sikora, K. *Clin. Oncol.* **2021**, *33*, e73−e81.

(11) Studdert, D. M.; Hall, M. A. *N. Engl. J. Med.* **2020**, *383*, 102−104.

(12) Suthar, M. S.; Zimmerman, M. G.; Kauffman, R. C.; Mantus, G.; Linderman, S. L.; Hudson, W. H.; Vanderheiden, A.; Nyhoff, L.; Davis, C. W.; Adekunle, O.; Affer, M.; Sherman, M.; Reynolds, S.; Verkerke, H. P.; Alter, D. N.; Guarner, J.; Bryksin, J.; Horwath, M. C.; Arthur, C. M.; Saakadze, N.; Smith, G. H.; Edupuganti, S.; Scherer, E. M.; Hellmeister, K.; Cheng, A.; Morales, J. A.; Neish, A. S.; Stowell, S. R.; Frank, F.; Ortlund, E.; Anderson, E. J.; Menachery, V. D.; Rouphael, N.; Mehta, A. K.; Stephens, D. S.; Ahmed, R.; Roback, J. D.; Wrammert, J. *Cell Rep. Med.* **2020**, *1*, 100040.

(13) Larsen, S. E.; Berube, B. J.; Pecor, T.; Cross, E.; Brown, B. P.; Williams, B. D.; Johnson, E.; Qu, P.; Carter, L.; Wrenn, S.; Kepl, E.; Sydeman, C.; King, N. P.; Baldwin, S. L.; Coler, R. N. *J. Immunol. Methods* **2021**, *499*, 113160.

(14) Cai, X.-f.; Chen, J.; Hu, J.-l.; Long, Q.-x.; Deng, H.-j.; Fan, K.; Liao, P.; Liu, B.-z.; Wu, G.-c.; Chen, Y.-k.; Li, Z.-j.; Wang, K.; Zhang, X.-l.; Tian, W.-g.; Xiang, J.-l.; Du, H.-x.; Wang, J.; Hu, Y.; Tang, N.; Lin, Y.; Ren, J.-h.; Huang, L.-y.; Wei, J.; Gan, C.-y.; Chen, Y.-m.; Gao, Q.-z.; Chen, A. m.; He, C.-l.; Wang, D.-X.; Hu, P.; Zhou, F.-C.; Huang, A.-l.; Liu, P.; Wang, D.-q., A Peptide-Based Magnetic Chemiluminescence Enzyme Immunoassay for Serological Diagnosis of Corona Virus Disease 2019 (COVID-19). medRxiv: 2020.02.22.20026617, **2020**.

(15) Bahadır, E. B.; Sezgintürk, M. K. *TrAC, Trends Anal. Chem.* **2016**, *82*, 286−306.

(16) Majdinasab, M.; Sheikh-Zeinoddin, M.; Soleimanian-Zad, S.; Li, P.; Zhang, Q.; Li, X.; Tang, X.; Li, J. *Food Control* **2015**, *47*, 126−134.

(17) Li, L.; Zhou, L.; Yu, Y.; Zhu, Z.; Lin, C.; Lu, C.; Yang, R. *Diagn. Microbiol. Infect. Dis.* **2009**, *63*, 165−172.

(18) Wang, P.; Wang, R.; Zhang, W.; Su, X.; Luo, H. *Biosens. Bioelectron.* **2016**, *77*, 866−870.

(19) Taranova, N. A.; Berlina, A. N.; Zherdev, A. V.; Dzantiev, B. B. *Biosens. Bioelectron.* **2015**, *63*, 255−261.

(20) Beloglazova, N. V.; Speranskaya, E. S.; Wu, A.; Wang, Z.; Sanders, M.; Goftman, V. V.; Zhang, D.; Goryacheva, I. Y.; De Saeger, S. *Biosens. Bioelectron.* **2014**, *62*, 59−65.

(21) Liu, Y.; Zhang, Z.; Wang, Y.; Zhao, Y.; Lu, Y.; Xu, X.; Yan, J.; Pan, Y. *Int. J. Food Microbiol.* **2015**, *211*, 109−116.

(22) Cai, Y.; Yan, J.; Zhu, L.; Wang, H.; Lu, Y. *Biosensors* **2020**, *10*, 161.

(23) Burr, D. S.; Fatigante, W. L.; Lartey, J. A.; Jang, W.; Stelmack, A. R.; McClurg, N. W.; Standard, J. M.; Wieland, J. R.; Kim, J.-H.; Mulligan, C. C.; Driskell, J. D. *Anal. Chem.* **2020**, *92*, 6676−6683.
(24) Chen, H.; Park, S.-G.; Choi, N.; Moon, J.-I.; Dang, H.; Das, A.; Lee, S.; Kim, D.-G.; Chen, L.; Choo, J. *Biosens. Bioelectron.* **2020**, *167*, 112496.
(25) Chen, S.; Meng, L.; Wang, L.; Huang, X.; Ali, S.; Chen, X.; Yu, M.; Yi, M.; Li, L.; Chen, X.; Yuan, L.; Shi, W.; Huang, G. *Sens. Actuators, B* **2021**, *348*, 130706.
(26) Li, J. F.; Huang, Y. F.; Ding, Y.; Yang, Z. L.; Li, S. B.; Zhou, X. S.; Fan, F. R.; Zhang, W.; Zhou, Z. Y.; Wu, D. Y.; Ren, B.; Wang, Z. L.; Tian, Z. Q. *Nature* **2010**, *464*, 392−395.
(27) Rycenga, M.; Xia, X.; Moran, C. H.; Zhou, F.; Qin, D.; Li, Z.-Y.; Xia, Y. *Angew. Chem., Int. Ed.* **2011**, *50*, 5473−5477.
(28) Huang, W.; Guo, E.; Li, J.; Deng, A. *Analyst* **2021**, *146*, 296−304.
(29) Li, D.; Zhao, J.; Ma, J.; Yang, H.; Zhang, X.; Cao, Y.; Liu, P. *Colloids Surf., B* **2022**, *211*, 112330.
(30) Liu, H.; Liu, T.; Zhang, L.; Han, L.; Gao, C.; Yin, Y. *Adv. Funct. Mater.* **2015**, *25*, 5435−5443.
(31) Qiu, Z.; Xue, Y.; Li, J.; Zhang, Y.; Liang, X.; Wen, C.; Gong, H.; Zeng, J. *Chin. Chem. Lett.* **2021**, *32*, 2807−2811.
(32) Zeng, J.; Li, M.; Liu, A.; Feng, F.; Zeng, T.; Duan, W.; Li, M.; Gong, M.; Wen, C. Y.; Yin, Y. *Adv. Funct. Mater.* **2018**, *28*, 1800515.
(33) Khlebtsov, N. G.; Lin, L.; Khlebtsov, B. N.; Ye, J. *Theranostics* **2020**, *10*, 2067−2094.
(34) Wan, Y.; Guo, Z.; Jiang, X.; Fang, K.; Lu, X.; Zhang, Y.; Gu, N. *J. Colloid Interface Sci.* **2013**, *394*, 263−268.
(35) Wang, C.; Yang, X.; Gu, B.; Liu, H.; Zhou, Z.; Shi, L.; Cheng, X.; Wang, S. *Anal. Chem.* **2020**, *92*, 15542−15549.
(36) Zeng, H.; Wang, J.; Jia, J.; Wu, G.; Yang, Q.; Liu, X.; Tang, X. *Food Chem.* **2021**, *335*, 127627.
(37) Tan, G.; Zhao, Y.; Wang, M.; Chen, X.; Wang, B.; Li, Q. X. *Food Chem.* **2020**, *311*, 126055.
(38) Kim, H.-Y.; Lee, J.-H.; Kim, M. J.; Park, S. C.; Choi, M.; Lee, W.; Ku, K. B.; Kim, B. T.; Changkyun Park, E.; Kim, H. G.; Kim, S. I. *Biosens. Bioelectron.* **2021**, *175*, 112868.
(39) Nam, J.-M.; Oh, J.-W.; Lee, H.; Suh, Y. D. *Acc. Chem. Res.* **2016**, *49*, 2746−2755.
(40) Ho, C.-H.; Lee, S. *Colloids Surf., A* **2015**, *474*, 29−35.
(41) Orendorff, C. J.; Gole, A.; Sau, T. K.; Murphy, C. J. *Anal. Chem.* **2005**, *77*, 3261−3266.
(42) Liu, P.-p.; Zong, Y.; Jiang, S.-p.; Jiao, Y.-j.; Yu, X.-j. *ACS Omega* **2021**, *6*, 9667−9671.
(43) Luo, S.; Xu, J.; Cho, C. Y.; Zhu, S.; Whittaker, K. C.; Wang, X.; Feng, J.; Wang, M.; Xie, S.; Fang, J.; Huang, A. S.; Song, X.; Huang, R.-P., *Quantitative Detection of Anti-SARS-CoV-2 Antibodies Using Indirect ELISA*; Laboratory Medicine, 2021.
(44) Lijia, S.; Lihong, S.; Huabin, W.; Xiaoping, X.; Xiaodong, L.; Yixuan, Z.; Pin, H.; Yina, X.; Xiaoyun, S.; Junqi, W. *J. Clin. Lab. Anal.* **2020**, *34*, No. e23466.
(45) Edouard, S.; Colson, P.; Melenotte, C.; De Pinto, F.; Thomas, L.; La Scola, B.; Million, M.; Tissot-Dupont, H.; Gautret, P.; Stein, A.; Brouqui, P.; Parola, P.; Lagier, J. C.; Raoult, D.; Drancourt, M., Evaluating the Serological Status of COVID-19 Patients Using an Indirect Immunofluorescent Assay, France. medRxiv 2020.05.05.20092064, **2020**.
(46) Yakoh, A.; Pimpitak, U.; Rengpipat, S.; Hirankarn, N.; Chailapakul, O.; Chaiyo, S. *Biosens. Bioelectron.* **2021**, *176*, 112912.
(47) Song, D.; Liu, J.; Xu, W.; Han, X.; Wang, H.; Cheng, Y.; Zhuo, Y.; Long, F. *Talanta* **2021**, *235*, 122800.
(48) Ahmadi, A.; Mirzaeizadeh, Z.; Omidfar, K. *Monoclonal Antibodies Immunodiagn. Immunother.* **2021**, *40*, 210−218.
(49) Bayin, Q.; Huang, L.; Ren, C.; Fu, Y.; Ma, X.; Guo, J. *Talanta* **2021**, *227*, 122207.
(50) Chen, Z.; Zhang, Z.; Zhai, X.; Li, Y.; Lin, L.; Zhao, H.; Bian, L.; Li, P.; Yu, L.; Wu, Y.; Lin, G. *Anal. Chem.* **2020**, *92*, 7226−7231.
(51) Liu, H.; Dai, E.; Xiao, R.; Zhou, Z.; Zhang, M.; Bai, Z.; Shao, Y.; Qi, K.; Tu, J.; Wang, C.; Wang, S. *Sens. Actuators, B* **2021**, *329*, 129196.
(52) Srivastav, S.; Dankov, A.; Adanalic, M.; Grzeschik, R.; Tran, V.; Pagel-Wieder, S.; Gessler, F.; Spreitzer, I.; Scholz, T.; Schnierle, B.; Anastasiou, O. E.; Dittmer, U.; Schlücker, S. *Anal. Chem.* **2021**, *93*, 12391−12399.

https://doi.org/10.1021/acs.analchem.2c01286
Anal. Chem. 2022, 94, 8466−8473